Digest Journal of Nanomaterials and Biostructures Vol. 19, No. 4, October-December 2024, p. 1517-1531

Ni substituted aluminum doped zinc titanate (AZNT) nano-particles: synthesis and characterization

Y. Srinivas[a], N. V. Krishna Prasad[a,*], U Naresh[b]
[a]*Dept. of Physics (GSS) Gitam Deemed to be University Bangalore, India*
[b]*Dept. of Physics, PVKK Institute of Technology, Anantapur, India*

We synthesized a series of Nickel-substituted Aluminium doped Zinc Titanate (AZNT) nano-particles using hydrothermal method. The structure of synthesized samples was meticulously analyzed using X-ray diffractometer (XRD) while the lattice parameters, crystallite size and volume were calculated with utmost precision. The morphology was further examined using two advanced microscopy techniques Field Emission Scanning Electron Microscopy (FESEM) and Transmission Electron Microscopy (TEM). These techniques provide detailed imaging and analysis of nano-scale materials. FESEM involves usage of electron beam to scan the surface of a sample and the sample's grain size was estimated. The study investigated the dielectric properties within a frequency range of 10Hz to 50MHz. The dielectric constants and impedance parameters were analyzed. The physical properties of the samples, as determined through these methods, hold promise for practical applications in super capacitors and energy storage devices, offering a glimpse into a potentially transformative future in energy technology.

(Received July 23, 2024; Accepted October 15, 2024)

Keywords: Ni substituted Al doped zink titanate (AZNT), XRD, FESEM, Dielectric properties

1. Introduction

In recent years, titanium dioxide (TiO_2) has gained significant attention as a material in view of its dual effect, such as being an active metal and reducible support. This study explores the potential of nickel substituted aluminium-doped zinc titanate nano-particles(AZNT), a material that could revolutionize capacitors with high energy storage, infrared detectors, ultrasonic sensors,electro-optic devices etc.[1-2]. Titanium dioxide's excessive availability in nature, high stability, nontoxicity, and cost-effectiveness make it a crucial component in these applications.

Observations indicated that perovskite materials, which are composites of titanium oxide, exhibit various remarkable properties that include chemical, structural, electrical and magnetic etc.[3]. These materials were discovered by Gustav Rose discovered in 1839 in Ural Mountains of Russia and named it after Russian mineralogist L.A.Perovski (1792-1856). The general formula for perovskite is ABO_3. In this structure, 'A' and 'B' represent two cations or positively charged ions, often of different sizes. The negatively charged ion 'O' (typically oxide) forms bonds with both cations. Generally, 'A' atoms have more significance than 'B' atoms. In an ideal cubic structure, 'B' cation is surrounded by an octahedron of anions in 6-fold coordination, while 'A' cation is in 12-fold coordination of cuboctahedra based on A and B element composition. Various composites such as $XTiO_3$ (where X= Ba, Ni, Mg, Sr, Pb, Al, La, Ca, Zn etc. belong to familiar parent materials. In addition to that, perovskites have been the subject of extensive research using a range of synthesis techniques such as solid-state reaction, sol-gel, auto-combustion, polyol, hydrothermal, and solvothermal methods. Notably, the hydrothermal technique has garnered attention as a promising approach due to its practicality and economic advantages [5].

Aluminium titanate is capable of withstanding corrosion from alkalis and hot salts due to its high melting point. It also does not get wet when in contact with molten glass. Compared to spinel and other host matrices, aluminium titanate was more resistant to corrosion from glass melt with

* Corresponding author: vnarasip@gitam.edu
https://doi.org/10.15251/DJNB.2024.194.1517

higher temperature stability. Unlike ceramic host matrices that contain baddeleyite and cassiterite, aluminium titanate unquestionably shares the same crystal structure as pseudo brookite. The unique orthogonal structure of aluminium titanate, featuring a space group of Z=4, showcases two highly distorted octahedra that host aluminium (III) and titanium (IV) cations. By strategically substituting these cations with high concentrations of different colourising ions, we can significantly boost the colouring power, resulting in a strikingly intense colouring effect [5]. The coordination between octahedrons [AlO_6] and [TiO_6] form the structural units of aluminium titanate crystals. These octahedrons are distributed in random and are cross-connected in co-top or co-edge structure forming aluminium titanate. Aluminium titanate is commonly used in various industries along with environmental protection. Research on aluminium titanates continue to expand their uses in batteries, dielectrics, photocatalysts, and ceramic membranes [6].

Aluminium titanate received significant attention due to its versatile, pigment-based applications in energy storage and catalysis. One of the main applications of aluminium titanate in energy storage is the production of lithium-ion batteries. Aluminium titanate can be used as a cathode material in these batteries to provide high energy density, durability with enhanced safety. It has excellent thermal stability and good electrical conductivity, making it a suitable material for high-performance batteries. Another critical application of aluminium titanate is in catalysis. It can be used as a catalyst support, providing a high surface area for the deposition of active species. Aluminium titanate exhibits excellent thermal stability and resistance to chemical corrosion, making it suitable for catalytic processes that involve high temperatures and harsh environments. It can be used in various catalytic reactions, such as the oxidation of organic compounds, conversion of harmful gases, and reduction of pollutants. Additionally, aluminium titanate has been explored for its potential in the production of pigments. Its unique crystal structure and composition allow for vibrant colours, especially when doped with various transition metals or rare earth elements [6]. These pigments find applications in ceramics, coatings, paints, and other industries where high-quality colouration is desired. Furthermore, aluminium titanate is being investigated for its potential in various other applications. Its low coefficient of thermal expansion makes it suitable for use in precision machinery, optical equipment, and electronic components. It also exhibits good thermal shock and mechanical stress resistance, making it a potential candidate for use in high-temperature furnace linings and refractory materials [7].

However, some limitations of aluminium titanate in battery applications may include its low energy density. Aluminium titanate may have a lower energy density than other battery materials, such as lithium-ion. This means the battery may not store as much energy and may have a shorter lifespan before recharging. Another factor is Poor conductivity: Aluminium titanate may have lower electrical conductivity than other battery materials. This can lead to slower charge and discharge rates, limiting the battery's ability to deliver high power output. Other factors include Limited cycling stability (capacity loss over repeated charge and discharge cycles, leading to decreased battery performance over time). Like other lithium-containing battery materials, aluminium titanate may pose a safety risk due to potential flammability and thermal runaway issues. This can impact its usage in specific applications where safety is critical [8]. Overall, while aluminium titanate shows potential for battery applications, it faces several challenges that must be addressed to be competitive with existing battery technologies.

Zinc titanate ($ZnTiO_3$) has attracted considerable attention in electrochemical reactions because of its redox properties, flexibility in composition, chemical stability, and cost-effectiveness. Introducing bimetallic support in $ZnTiO_3$ perovskite and combining it with nickel holds promise in electrochemical reactions. Researchers have studied the creation of a composite of NiO and TiO_2-supported $ZnTiO_3$ for continuous hydrogen production.[9].

$ZnTiO_3$ is emerging as a highly promising candidate for low-temperature ceramics due to its advantageous dielectric properties, including a low dielectric loss and high dielectric constant, as well as its ability to sinter at lower temperatures. The synthesis of zinc titanates in their nanocrystalline form may offer the potential to further lower the sintering temperature for microwave dielectrics, eliminating the need for external agents[10].

Many researchers have investigated nickel-doped zinc titanate and aluminium titanate. For instance, Niti et al. [11] reported that the Ni doped Lead Zirconate Titanate ceramics pellets exhibited the highest dielectric constant with Ni content ranging from 0 to 20. The prepared ceramics

were tested for their dielectric constant values (ε') and tanδ in relation to frequency and temperature. The results indicated highest dielectric constant ever reported for Ni-doped PZT with a doping of 5 at.%. With increase in doping concentration of Ni, the maximum dielectric constant value decreased with an upward trend in phase transition temperature. Chen et al. [12] conducted a study in which they substituted nickel ions with Al^{3+} in aluminum titanate lattice, effectively doping the lattice with Ni^{2+}. This doping decreased the distortion of the octahedral structure, leading to a significant colouration effect and a substantial improvement in the synthesis and stabilisation of aluminium titanate. Kim et al. [13] used the solid-state reaction route synthesised dielectric ceramics in the system $(Zn_{1-x}Ni_x)$ TiO_3, x = 0 to 1. The phase distribution, microstructure, and dielectric properties were characterised using powder X-ray diffraction analysis, electron microscopy, and microwave measurement techniques. Kongming et al. [14] prepared piezo catalysis that directly converts mechanical vibrations can be converted into chemical energy. In this study, $NiTiO_3$ is being used for the first time in photocatalytic hydrogen evolution. The non-central symmetry of $NiTiO_3$ is enhanced by doping it with significant radius elements. The research demonstrates that when a metal element replaces the nickel sites, it leads to lattice distortion and a higher piezoelectric response. Sakout et al. [15] prepared $(Zn_{0.16}Ba_{0.16}Ca_{0.16}Sr_{0.16}La_{0.33})$ $Ti_{1-x}Al_xO_3$ $(0 \leq x \leq 0.1)$ composite for the application of high entropy materials which having extreme dielectric constant through the simple solid-state reaction determined 1300°C to 1400°C by adding Zinc, Barium, calcium, strontium and lanthanum titanate for microwave dielectric processes. It concluded that the Al element is good for the variation of the dielectric constant. Their work provided a practical approach to improving the properties of microwave dielectric ceramics. However, it is essential to note that $ZnTiO_3$ is not a commonly studied compound, and limited information is available specifically on the effects of nickel incorporation. Adding nickel may induce structural changes in $ZnTiO_3$, altering its crystal structure. This can lead to different physical properties compared to pure $ZnTiO_3$.

Nickel doping can introduce charge carriers into the $ZnTiO_3$ compound, increasing electrical conductivity. This can make Ni-doped $ZnTiO_3$ potentially useful for applications that require improved electrical conductivity, and This may result in interesting magnetoelectric effects and potential applications in spintronics. The $ZnTiO_3$ is known for its optical properties, such as transparency in the visible range. Adding nickel may affect the optical bandgap and absorption properties, potentially altering its optical characteristics. Thermoelectric Properties also have significant variations by nickel doping, such as the Seebeck coefficient and electrical conductivity, leading to enhanced thermoelectric performance for energy conversion applications.

This study seeks to investigate the presence and stability of ordered rhombohedral titanates of Nickel in combination with various transition metals. The arrangement of the synthesis procedure is crucial in establishing the crystal structure of complex Ni-titanates, and it also elucidates the crystal structure evolution resulting from the incorporation of Nickel with other transition metals. The study highlights the influence of compositionally driven phase transitions in the $Al_{0.8}Zn_{0.2-x}Ni_xTiO_3$ compounds involving Nickel. Additionally, the authors expanded the research by introducing Ni into the ternary aluminium zinc titanate $Al_{0.8}Zn_{0.2-x}Ni_xTiO_3$ (x= 0.04, 0.08, 0.12, 0.16) nanoparticles and analyzed their structure and dielectric properties.

2. Synthesis

Nickel nitrate $Ni(NO_3)_2$, aluminium nitrate $Al(NO_3)_2$, zinc nitrate $Zn(NO_3)_2$, titanium oxide TiO_2, and ammonium hydroxide NaOH chemicals were purchased from Sigma-Aldrich are used to synthesise compounds such as $Al_{0.8}Zn_{0.16}Ni_{0.04}TiO_3$, $Al_{0.8}Zn_{0.12}Ni_{0.08}TiO_3$, $Al_{0.8}Zn_{0.08}Ni_{0.12}TiO_3$, and $Al_{0.8}Zn_{0.04}Ni_{0.16}TiO_3$, which have the general formula $Al_{0.8}Zn_{1-x}Ni_xTiO_3$ (x= 0.04, 0.08, 0.12, 0.16) or AZNT nanoparticles. The procedure followed as the chemicals were dispersed in 50 mL deionised water as per the planned stoichiometric ratio as per the formula $Al_{0.8}Zn_{0.2-x}Ni_xTiO_3$ zinc nitrate dispersed in 50 mL deionised water was mixed with ammonium hydroxide until a pH 11 was achieved. The solution was moved to a 100 mL Teflon autoclave, heated to 120°C for 12 hours, and dried overnight at 100°C. The resulting product underwent calcination for five hours at 100°C, followed by natural cooling. The same procedure was followed for different amounts of nickel

nitrate 0.04, 0.08, 0.12, and 0.16 wt% were added to $Al_{0.8}Zn_{0.2-X}Ni_xTiO_3$, this solution having different concentrations was stirred separately at ~25 °C for five hours and dried in an oven for 24 hours. The entire process continued for all the composite samples. The obtained material sample was characterised using Field Emission Scanning Electron Microscopy, X-ray diffraction, and Transmission Electron Microscopy techniques to determine the crystal structure and morphology and the dielectric properties checked with the impedance analyser.

3. Results and discussion

3.1. X-ray diffraction (XRD)

The X-ray diffraction patterns, as illustrated in Figure 1, are utilized to ascertain the phase, crystallinity and structure among other characteristics.

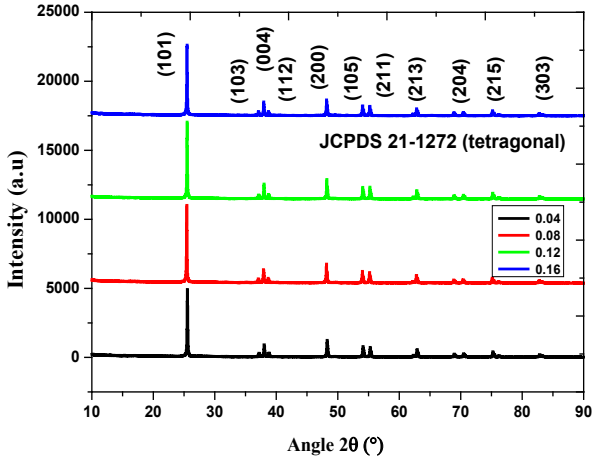

Fig. 1 XRD of AZNT particles.

All samples of AZNT show good crystalline structure. The most substantial diffraction peak occurs at an angle of 25.314^0 for a range of concentration x = 0.04–0.16. We compared all the peak positions with a standard reference and found that the resulting phases are related to a tetragonal structure. Additionally, we calculated the average size of the crystals using the Debye-Scherrer formula.

$$D_a = \frac{0.9\lambda}{\beta \cos\theta}$$

The full-width half maxima (FWHM) denoted as β, is a parameter. The wavelength of the CuKα source is represented by λ and is equal to 0.15406 nm. The diffraction angle is denoted as θ. The information presented in Table 1 indicates that the change in FWHM ranges from 0.2185 to 0.4322 radians, as a result, the crystallite size 'Da' fluctuates between 59 and 50 nm depending on composition. Consequently, the tetragonal unit cell dimensions are calculated using the equation:

$$\frac{1}{d^2} = \frac{h^2 + \mathrm{k}^2}{a^2} + \frac{l}{c^2}$$

In the above equation, the inter planar distance is represented by 'd', Miller indices by (h k l) and the findings indicated a decrease in lattice parameters a and b from 4.3–4.7 Å, and parameter c decreased from 4.9–5.2 Å with an increase in Ni content. The unit cell volume is calculated using

the well-known formula. Using the lattice parameters $\frac{c}{a}$ ratio was calculated. The c/a ratio in a tetragonal lattice refers to the ratio between the unit cell's height (c-axis) and base length (a-axis). In a tetragonal lattice, the c/a ratio is typically greater than 1, meaning the c-axis is longer than the a-axis. The exact value of the c/a ratio depends on the specific lattice structure and can vary for different materials.

It is worth noting that the c/a ratio can significantly influence the physical properties and behavior of materials with a tetragonal lattice, such as their mechanical, electrical, or thermal properties. Hear, and it was observed that this ratio was 1.13 to 1.10 concerning a substation of nickel concentrations. Obtaining values greater than one was in excellent agreement with the calculated lattice parameters a and b, which were always less than c.

$$V = a^2 c$$

where 'a' and 'c' are lattice parameters

As the composition changed, the range of calculated volumes decreased from 90.60 to 114.86 Å3. This variation in lattice parameters is attributed to the Shannon ionic radii data of the cations in the nickel element, providing a detailed understanding of the underlying factors influencing the observed changes. The ionic radii of cations that have been used in this work are given as Ni^{+2}: 1.24 Å, Al^{+2}: 1.43 Å, Ti^{+4}: 0.68 Å and Zi: 1.38 Å [23]. The ionic radii of cations Ni^{+2}, Al^{+2}, Zi^{+2} and Ti^{+4}, The ionic radius of Nickel is smaller than that of Aluminium and Zinc cations. As a result, when Nickel is substituted for Zinc, the lattice parameters and structural changes exhibit minimal variation with increasing Nickel content.

X-ray density (ρ_x) is evaluated from the relation:

$$\rho_x = \frac{ZM}{NV}$$

where N denote Avogadro's number, 'V' the unit cell volume and 'M' represent compositional molecular weight.

The data obtained from the experiment indicates a marked increase in density from 3.71 to 3.44 g/c.c. A corresponding increase as denoted by 'x', is observed. This change in density is commonly associated with the concurrent increase in value of 'M' from 219.709 to 222.500 g/mol. The specific surface area is calculated using the equation

$$S = \frac{6000}{Da\ \rho x}.$$

In Table 1, we have documented the parameters "Da," representing the crystallite size, and " ρ_x," representing the X-ray density. The observed changes range from 0.027 to 0.038 g/cm^3, and this variability seems to have an inverse relationship with "Da" [23]. Previous literature also shows similar patterns [24]. To calculate the theoretical density of a material, one can consider its atomic or molecular structure, considering atomic weights and crystal structure. On the other hand, the actual experimental density or bulk density is measured.

$$\rho_e = \pi r^2 t$$

where m, r, and t represent the pellets' mass, radius, and thickness, respectively. The bulk density of materials exhibited a similar trend to that of the theoretical density. Several factors can influence the differences between titanate composites' theoretical and accurate densities. These factors encompass the materials' impurities, crystal structure variations, porosity, and manufacturing techniques. Additionally, doped elements in prepared composites and impurities in the materials can contribute to the disparities between theoretical and accurate densities. In summary, the variations in densities of these materials can be traced back to a combination of factors related to their composition, structure, and the processes involved in their manufacturing.[24]. Using the theoretical density ρ_t and experimental density ρ_e the porosity was determined using the relation

$$P = 1 - \frac{\rho_e}{\rho_t}$$

The porosity measures the empty spaces or voids within a material. It is a property that indicates how much fluid, such as water or air, a material can hold or allow to pass through. Porosity is expressed as a percentage and can vary depending on the type of material. A highly porous material will have more void spaces, while a less porous material will have fewer. Porosity is an essential characteristic in various fields, including geology, engineering, and materials science, as it affects a substance's permeability, strength, and other properties.

Table 1. Structural parameters of AZNT nano-particles.

x	**0.04**	**0.08**	**0.12**	**0.16**
a =b (nm)	4.3	4.1	4.2	4.7
c (nm)	4.9	4.2	4.8	5.2
c/a	1.1395	1.0243	1.1428	1.1063
D (nm)	59	58	51	50
V	90.60	70.60	84.67	114.86
ρ_x (g/cm^3)	3.7151	5.0559	4.4472	3.4487
ρ_e (g/cm^3)	3.2321	4.1458	3.3799	2.1382
porosity (P)	0.13	0.18	0.24	0.38
Grain size	151.6	153.6	152	128
S (m^2/g)	0.0273	0.0204	0.0264	0.0347

3.2. Morphological properties

The surface morphology of AZNT samples was analysed using FESEM and TEM images. The FESEM images of x = (0.04, 0.08, 0.012, and 0.16) content display clustered grains with small sphere structures, as seen in Figure 2 with the increase of Ni-content from 0.04 to 0.16, the formation of Flower petals increases and spheres decreases; meanwhile, the formation of spheres decreases [25]. x = 0.16 content displays a well-defined flower-petal agglomerated structure. The average grain diameter is observed to increase for concentrations of 0.04 and 0.08 from 151.6 to 153.6, then decreased for contents 0.012 and 0.16 from 152nm to 128nm, while different analyses was observed where the grain sizes were reduced from 69.62 to 45.58 nm for x = 0.2 to 0.4 contents.

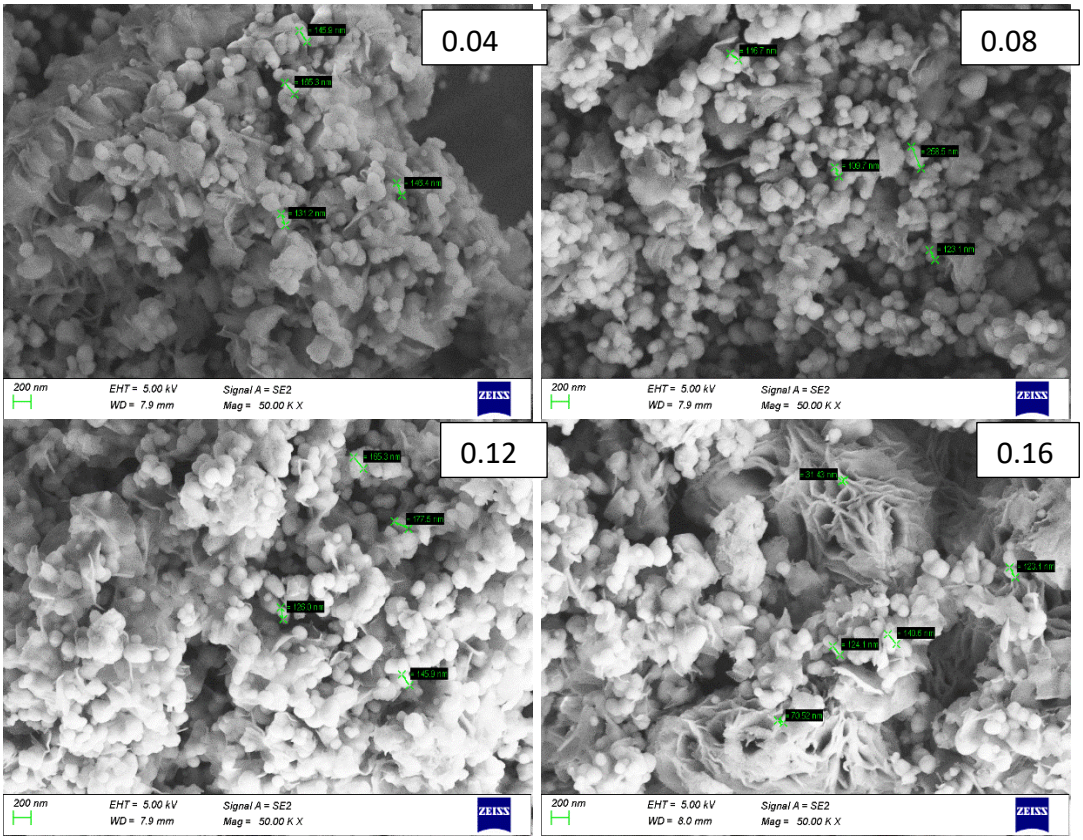

Fig. 2. FESEM Images of AZNT nanoparticles.

The transmission electron microscope (TEM) images in Figure 3 display the high-resolution nanostructures, revealing variations in the number and size of nanospheres with changes in Ni content. Specifically, at a Ni-content of x=0.04, complete and elongated particles in nanometres are observed. These findings provide photographic proof that the morphological properties of AZNT nanostructures are influenced by the increasing Ni-content in the $Al_{0.8}Zn_{0.2-x}Ni_xTiO_3$ perovskite system, leading to changes in the shape of the nanoparticles. This nano petal's structure is formed due to distortions upon substituting the Ni-element [26]. The level of distortion seems to go up as the nickel content increases. As a result, the spherical nanoparticles or grains undergo internal distortions, which deform their shape and cause secondary growth in preferred directions, leading to the development of petal-shaped nanostructures in their morphology. However, nanometals' dimensions are also developed after replacing the Ni^{2+} cations. These petals' nanostructure can potentially help electrodes in various applications. The unique size of spheres on petals can provide several advantages for electrode materials, including the Increased surface area of petals, which can provide a larger surface area compared to flat surfaces, enhancing the electrochemical reactions on the electrode. This can lead to higher efficiency and improved performance in energy storage and conversion devices like batteries and supercapacitors [27]. This can lead to lower resistance and improved conductivity, which is crucial for high-performance electrodes in energy storage and electrochemical devices.

They can facilitate specific electrochemical reactions, enabling faster and more efficient electrochemical processes in applications like fuel cells or water-splitting devices. The petals' nanostructures can also contribute to the stability and durability of the electrode material. They can prevent agglomeration of active materials, improve structural integrity, and enhance the resistance to chemical and mechanical degradation, resulting in longer electrode lifetimes. By leveraging the unique properties of petals' nanostructures, researchers can develop electrode materials with improved performance, efficiency, and stability for various electrochemical applications. However, it should be noted that translating these natural-inspired structures into practical electrode designs

involves careful material synthesis, characterisation, and optimisation to ensure their effectiveness in real-world applications [28].

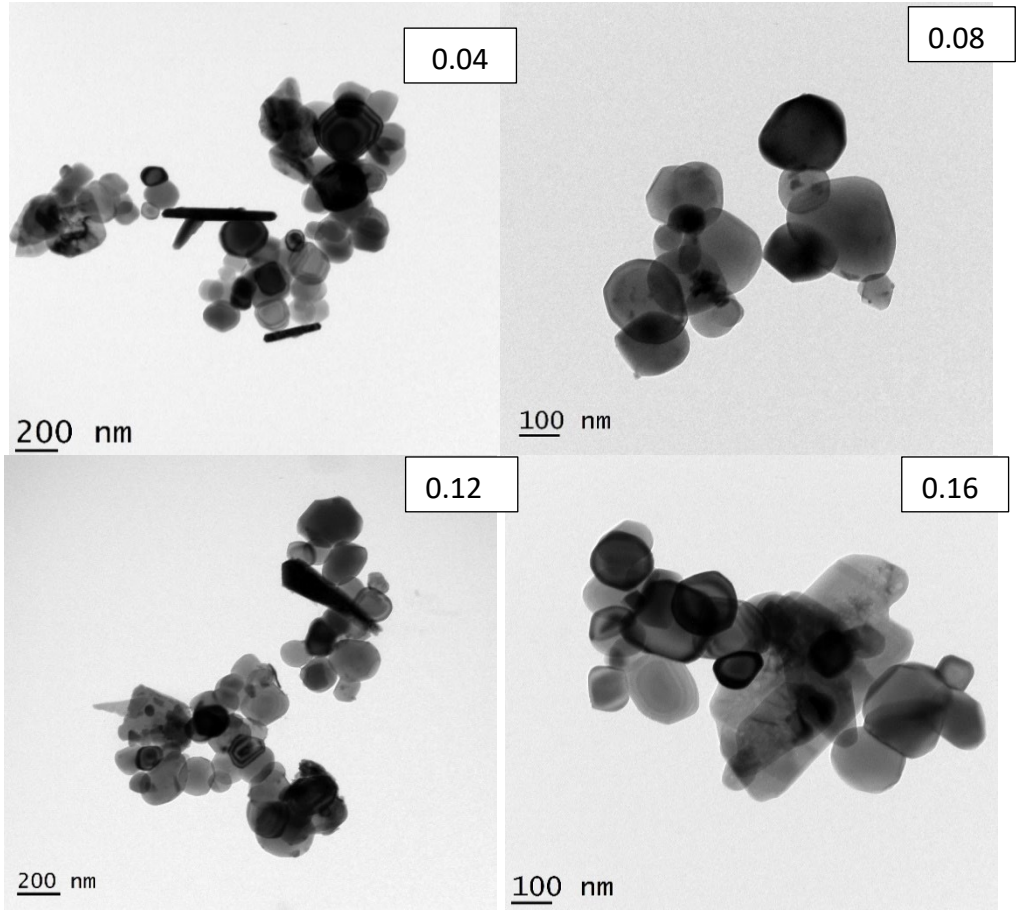

Fig. 3 TEM Images of AZNT nano-particles.

3.4. Dielectric properties

The graph shown in Figure 4 depicts the change in the real (ε′) and imaginary (ε″) dielectric constants for all AZNT nanoparticles in frequency (from 0 Hz to 50 MHz). It is evident that at lower frequencies, all compositions exhibit high values of ε′ and ε″. As the frequency increases, these values decrease. This behavior is consistent with Koop's theory or the two-layer model [29], which attributes it to polycrystalline materials' grain and grain boundaries. In this model, grain boundaries are high-resistance layers, while the grains are high-conductivity layers. The grain boundaries become more prevalent at lower frequencies and exhibit high resistance. At x=0.08, carriers with low dielectric constants exhibit reduced specific energy when subjected to a low-frequency electric field in all AZNT samples. These carriers are essential for mobility and tend to accumulate at the grain boundary interface. Consequently, the resistance of the grain boundary exceeds that of the carriers, causing an accumulation of carriers at the interface. Importantly, due to their lower energy levels compared to the grain boundaries, carriers are unable to traverse the grain boundary. As a result, a significant amount of polarisation is generated, known as Maxwell-Wagner's interfacial polarisation or space charge polarization. When the frequency is increased, the carriers gain extra energy compared to their original state. This causes some carriers to break through the grain boundary and move into the grain part of the material, leading to a decrease in the values of ε′ and ε″ of AZNT. At high frequencies, the ε′ and ε″ values for x = 0.04–0.08 are low, indicating that the cloud of charge carriers is disrupting grain boundaries. This allows the carriers to move through the grain segment without encountering opposing layers. This resembles the dielectric behavior

observed in various polycrystalline materials using the conventional/Debye model.[30], respectively, and at a higher frequency, the dielectric constant goes to negative.

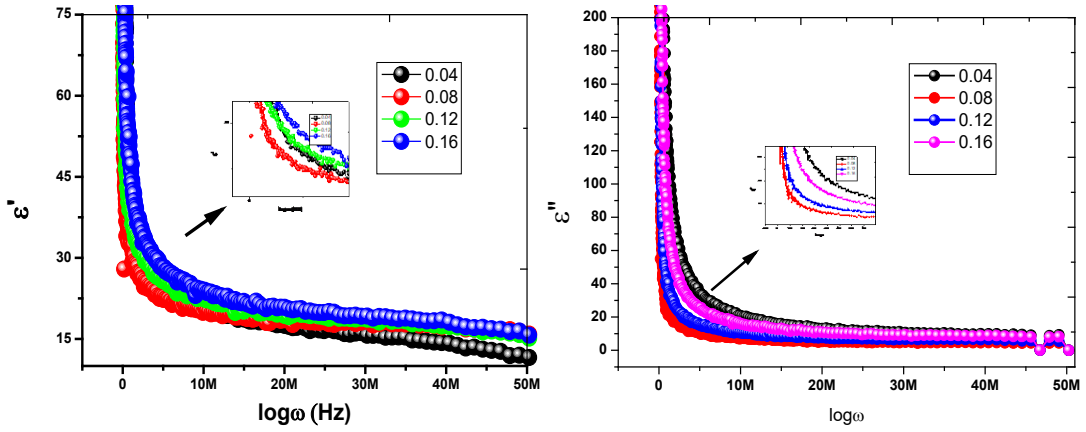

Fig. 4. Frequency dependence of ε' and ε'' for AZNT nano-rods.

Various materials can be used as dielectrics in capacitors, each with suitable dielectric constants. Some common dielectrics used in capacitors include Ceramic capacitors, which are commonly used due to their high dielectric constant and low cost. They are suitable for applications that require stable and reliable capacitance values. Aluminium oxide is widely used as a dielectric in electrolytic capacitors. It provides a high dielectric constant and can handle high voltages, making it suitable for applications that require large capacitance values and high voltage ratings. The choice of dielectric depends on the specific requirements of the capacitor's application, such as desired capacitance, operating voltage, temperature range, and size constraints. Hear the nickel-doped aluminum zink titanate ceramics having the positive dielectric constant (ε′) typically and is suitable for energy storage and a positive dielectric loss (ε″) suggests energy dissipation or emission; materials with high values of both ε′ and ε″ are well-suited for use in charge-stored capacitors and dielectric absorbers. This type of dielectric behavior aligns with the Debye model and can be observed in materials with x = 0.16 to 0.04 contents. Furthermore, it is notable that the electric displacement vector (D) aligns opposite the direction of the electric field (E). Electric displacement is a term used in electromagnetism to describe the overall effect of electric charges on a material [31]. It is denoted by the vector symbol D. It is calculated by adding the electric field vector E to the polarisation vector P, representing the material's electric dipole moments. The electric displacement vector always points in the opposite direction of the electric field vector. This means that if the electric field points toward one direction, the electric displacement vector will point in the opposite direction. The relation between D and E can be understood using the concept of free charges and bound charges. Free charges can move within a material, while bound charges are associated with aligning the electric dipole moments in the material. When a material is exposed to an external electric field, both free and bound charges within the material are displaced. The electric field and electric displacement vectors have opposite directions due to the polarization of bound charges, which creates an electric field that opposes the external field [30].

Additionally, the electric flux density is established in the opposite direction to the direction of E, resulting in negative polarisation and a negative value for the dielectric constant (epsilon). This behavior is like the diamagnetic nature of magnetic materials, where negative susceptibility arises from reverse magnetization. Negative dielectric loss leads to a greater amount of emission than absorption. This causes the electrons to act as if they are in a damped harmonic oscillator system, becoming free and accumulating at the surfaces of the pores within the material's interior, where they are affected by the orbitals. The dielectric materials uphold the energy conservation law. The energy is stored with the trapped electrons within the surfaces of the pores. Energy storage is a result of the separation of free electrons, but their positions are unstable. Consequently, the accumulated

energy will be emitted under specific applied frequency conditions. This phenomenon demonstrates the conservation of energy in the case of negative dielectric materials. Similar negative dielectric properties have been documented in the literature [27-28]. It is confirmed that x=0.04 content suits various microwave and radar absorber applications [28].

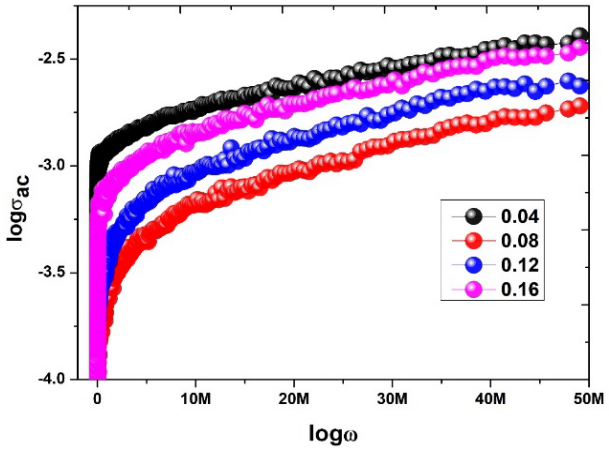

Fig. 5 The variation of ac-electrical conductivity (σ_{ac}) as a function of logω(Hz) for AZNT nanorods.

The graph in Figure 5 shows the relationship between ac-electrical conductivity (σ_{ac}) and logω(Hz) and observed that the conductivity is lower at lower frequencies because of the low thermal activation of the charge carriers. As the frequency increases, the conductivity shows a gradual increment, which can be attributed to the higher thermal activation of the charges. The nanorod structures demonstrate the apparent ac-conductivity of AZNT samples. The sample with x = 0.04 demonstrates clear petal structures with nanosphere inclusions. A high level of conductivity is anticipated for x = 0.04. The measured ac-electrical conductivity at 8 MHz is -9.07 X 10^{-2} S/m. A comparison indicates that the high conductivity of the x = 0.04 content can be attributed to its elongated nanorods in the microstructure.

The usual morphological forms, such as tiny spheres, flat shapes, and uneven rocks, usually result in a higher quantity of grain borders. In the current study, at x = 0.16, we observed structures resembling plates that have smooth grain borders, enabling electrons to participate in the electron hopping conduction process.

The complex dielectric modulus analysis in Figure 6 a is used to describe dielectric polarization behavior. Here, the complex dielectric modulus is represented as $M^*=M' + jM''$, where the real part is considered as $M'=\varepsilon'/(\varepsilon'^2+\varepsilon''^2)$ M'' is considered as the imaginary part and $M'' = \varepsilon''/(\varepsilon'^2+\varepsilon''^2)$. The formalism of the complex dielectric modulus is a fascinating and informative concept that elucidates the dielectric relaxation process, space charge effect, and polarization mechanism [33]. At low frequencies of log ω, the parameters M' and M'' decrease because of the long-range movement of charge carriers. During this phase, the carriers do not have a restoring force, causing M' and M'' to approach zero. A consistent pattern of M' and M'' is observed up to log ω = 5. After this point, there is a gradual increase in M' and M'', which is due to the short-range movement of carriers. The M' – log ω plots do not exhibit any relaxation dynamics, whereas the M'' – log ω plots indicate the presence of relaxation dynamics.

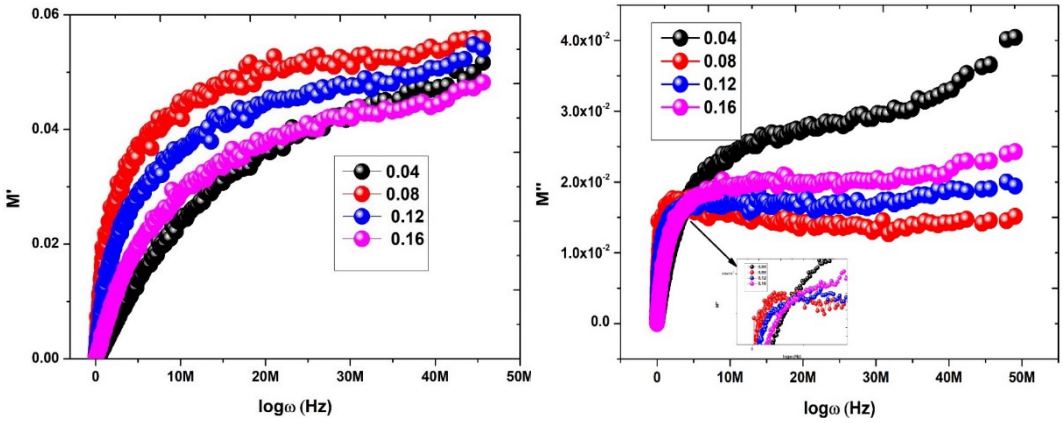

Fig. 6. Complex dielectric modulus analysis as a function of frequency for AZNT nanorods.

The data indicates a decrease in relaxation frequency with increasing frequency, suggesting non-Debye-type relaxations caused by mobile charges. At x = 0.04, there is a noticeable increase in M′ and M″ values above 89 kHz due to the polarization effect. Additionally, the inset of Figure 6 provides a clear illustration of the variation in M′ and M″ values at 90 kHz. When examining M″ – log ω plots, the relaxations can be categorized into long-range and short-range polarization regions. Long-range polarization results in long-range hopping conduction mechanisms occurring below the relaxation frequencies. These mechanisms stem from the extended motion of the carriers. Likewise, short-range polarization gives rise to short-range conduction mechanisms due to the confinement of carriers within the potential well [34].

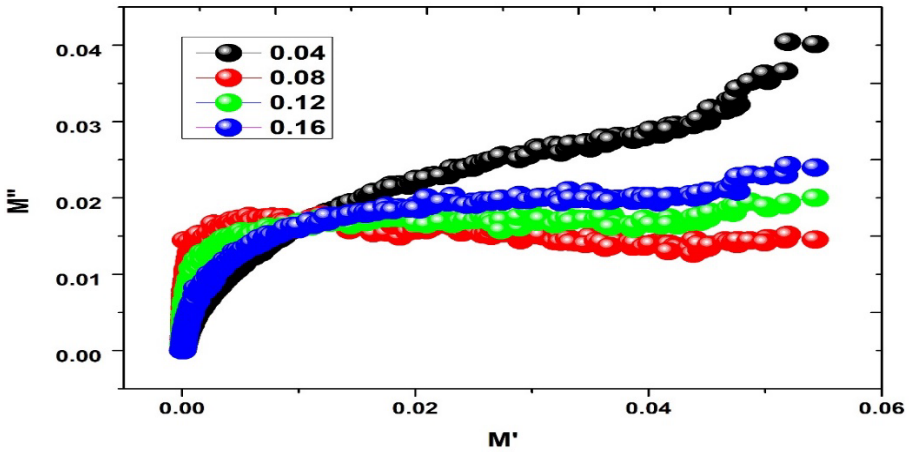

Fig. 7. M′ and M″ versus frequency for AZNT nano-rods.

In addition to the M′ versus M″ plots depicted in Figure.7, all AZNT compositions exhibited complete semicircular arcs, reflecting the grain contribution rather than the grain boundaries. The curved shapes showed that the strength in the materials was completely relaxed, and their centres were below the M′-axis, which means they didn't follow the usual relaxation pattern. [34].

Notably, for the x = 0.04 composition of AZNT nanorods, the arc formation was recorded in the direction of the M″-axis instead of the M′-axis, contrasting with the typical behaviour observed in conventional polycrystalline or dielectric materials. This is attributed to the reverse polarisation and dielectric behaviour of the x = 0.04 composition. Despite this deviation, this composition shows potential for high-frequency microwave absorber applications [35-36].

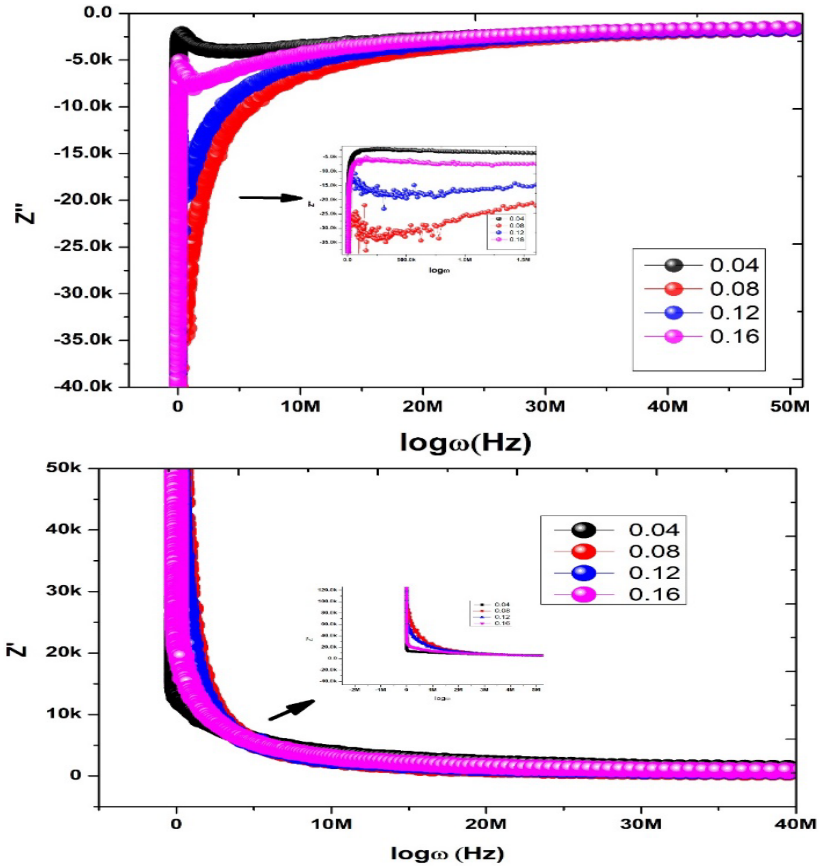

Fig. 8. Frequency dependence of Z' and Z'' for AZNT nano-rods.

The analysis of impedance spectroscopy provides valuable insights into the microstructure and electrical conduction mechanisms. By examining the complex impedance ($Z^* = Z' - jZ''$) as a function of log ω at room temperature, we can gain a deeper understanding of these mechanisms. Figure 8 illustrates the frequency dependence of Z' and Z''. At low log ω, we observe high magnitudes of Z' and Z'', indicating the presence of an inhomogeneous dielectric structure and highly resistive grain boundaries. These factors contribute to the observed phenomenon. In simpler terms, this is caused by the space charge effect at the interface [37], known as the space charge polarisation effect. As logω increases further, the Z' and Z'' values decrease in magnitude. The phenomenon is caused by the movement of charge carriers through the grain boundary layers, which enables them to move more freely within the grain portion, resulting in increased bulk conductivity. However, for x = 0.04, there is an interesting reversal in the Z' – logω and Z'' – log ω plots (refer to the inset figures of Fig. 8) observed between 8.9 kHz to 8 MHz. This is attributed to the dielectric behavior resulting from the negative polarization effect of the x = 0.04 content at the applied frequencies.

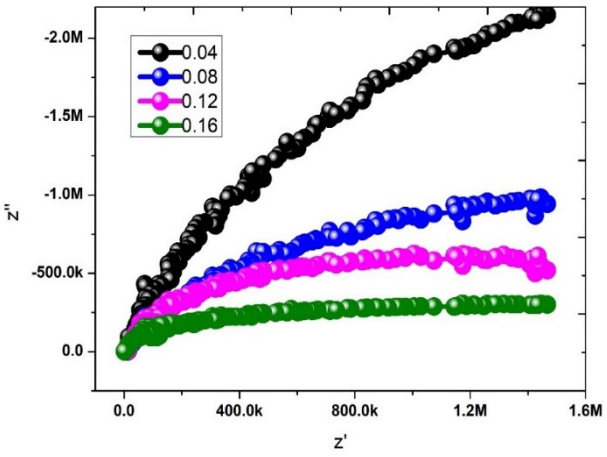

Fig. 9. Cole-Cole plots.

Furthermore, the low Z′ and Z″ values indicate a high conducting nature resulting from well-defined nanorods. Additionally, the Cole-Cole plots (Z′ versus Z″) shown in Fig. 9 illustrate the gradual formation of a semicircular arc with an increase in Ni-content. The arcs corresponding to values of x between 0.04 and 0.16 demonstrate partial formation, which is attributed to the partial relaxation strength, allowing carriers to move over longer distances. The carriers do not need to exert additional force to reach saturation.

The complete semicircular arc is formed for an x value of 0.04, indicating the movement of charges over shorter distances and their confinement to the potential well [38]. Additionally, the Cole-Cole plots for x values ranging from 0.12 to 0.16 exhibit distinct asymmetrical trends caused by defects, particle size, moisture, etc. The first arc in the Cole-Cole plots corresponds to the grain contribution, while the second arc reflects the contribution from grain boundaries. Our study's graphs clearly depict distinct arcs associated with the role of grains in electrical conduction. This behavior is intricately connected to the material's microstructure. The presence of nano-scale plate-like structures leads to smaller grain boundaries, which promotes electrical conduction through the grains to a greater extent [39]. After analyzing the plotted data, we can determine the bulk resistance by finding the intersection of the arc with the Z′-axis. As a result, the calculated bulk resistance for the material with x = 0.16 is 83.5 Ω. This indicates that the material with x = 0.16 demonstrates substantial bulk conductivity. Elongated nanostructures and high electrical conductivity are supported by x = 0.16. In the range of x = 0.04–0.16, non-Debye relaxations are detected as a result of the existence of arc centers below the Z′-axis [40].

4. Conclusion

The hydrothermal method was used to synthesize nickel-incorporated aluminum zinc titanate nanoparticles. The XRD analysis revealed a tetragonal structure with increased grain size due to nickel doping. The FESEM and TEM images showed a petal-like structure for the 0.16 content. This morphology is highly beneficial for electrode materials, and the studied dielectric properties support the application of these electrodes for batteries and supercapacitors.

References

[1] Kadiyala, Chandra Babu Naidu, Nagasamudram, Suresh Kumar, (2020), Materials Characterization. Volume 166, August 2020, 110425;
https://doi.org/10.1016/j.matchar.2020.110425

[2] Vanishree, P., Swati, G., J Mater Sci: Mater Electron 35, 597 (2024);
https://doi.org/10.1007/s10854-024-12350-9

[3] S. J. Mofokeng, L. L. Noto, T. P. Mokoena, T. A. Nhlapo, M. J. Sithole, M. Maswanganye, M. S. Dhlamini. (2023). Progress in Optical Science and Photonics, vol 25. Springer; https://doi.org/10.1007/978-981-99-4145-2_4

[4] Nagasamudram, Suresh Kumar. (2020), Journal of Materials Science Materials in Electronics. 31; https://doi.org/10.1007/s10854-020-03469-6

[5] T. Ramaprasad, R. J. Kumar, U. Naresh, M. Prakash, K. Chandra Babu Naidu, (2018) Materials Research Express 5 095025; https://doi.org/10.1088/2053-1591/aad860

[6] Dastagiri, S & Pakardin, G., Tadiboyina Phd, Anil Babu, Lakshmaiah, M., Naidu, K., (2021) Journal of Materials Science: Materials in Electronics. 32. 1-16; https://doi.org/10.1007/s10854-021-05525-1

[7] Devi, D., Kumari, P., Kumar, N., (2023), Journal of Materials Science: Materials in Electronics. 34; https://doi.org/10.1007/s10854-023-10608-2

[8] Law, C., Sofie, Stephen. (2011), Journal of The Electrochemical Society. 158. B113; https://doi.org/10.1149/1.3610226

[9] G.H. Khorrami, A.K. Zak, A. Kompany, Ceram. Int. 38 (2012) 5683-5690; https://doi.org/10.1016/j.ceramint.2012.04.012

[10] Huang, CW., Chen, RA., Chen, WY. et al., Top Catal 66, 34-40 (2023); https://doi.org/10.1007/s11244-022-01616-3

[11] 11] Nitu Kumari, Shagun Monga, Mohd. Arif, Neeraj Sharma, Arun Singh, Vinay Gupta, Paula M. Vilarinho, R.S. Katiyar, Ceramics International; https://doi.org/10.1016/j.ceramint.2018.11.117

[12] Junhua Chen, Guo Feng, Feng Jiang, Li Yin, Qianqian Zhao, Shanfang Lan, XiaoJun Zhang, Jianmin Liu, Qing Hu, Weihui Jiang, Ceramics International, Volume 47, Issue 23, 2021, Pages 33242-33251; https://doi.org/10.1016/j.ceramint.2021.08.225

[13] [13] Kim HT, Hwang J-C, Nam J-H, Choi BH, Lanagan MT, Journal of Materials Research. 2003;18(5):1067-1072; https://doi.org/10.1557/JMR.2003.0147

[14] Kongming Li, Bonan Li, Xi Zhang, Junhao Wu, Mengxue Chen, Pengfei Feng, Xu Yang, Meiyu Zhang, Yong Ding, Enhancement of NiTiO3 photocatalytic hydrogen evolution by doping with large radius elements; https://doi.org/10.1039/D4CC00889H

[15] Su, T., Chen, H., Wei, Z., Hao, M., Wang, X., Liu, Y., Ma, C., Miao, Y., Gao, F. (2023), Ceramics International; https://doi.org/10.1016/j.ceramint.2023.11.249

[16] Liferovich RP, Mitchell RH, (2004), Acta Crystallogr B60:496-50; https://doi.org/10.1107/S0108768104017963

[17] Mitchell RH, Liferovich RP, (2004), Can Mineral 42:1871-1880; https://doi.org/10.2113/gscanmin.42.6.1871

[18] Kubota, Y., Okamoto, Y., Kanematsu, T., Yajima, T., Hirai, D., Takenaka, K., (2022) Large Magnetic-Field-Induced Strains in Sintered Chromium Tellurides; https://doi.org/10.1063/5.0134911

[19] Li, J., Xu, J., Yu, S. et al., Polym. Bull. 80, 4245-4261 (2023); https://doi.org/10.1007/s00289-022-04255-6

[20] Wang, CL., Hwang, WS., Chu, HL. et al., Metall Mater Trans A 45, 2689-2698 (2014); https://doi.org/10.1007/s11661-014-2282-5

[21] U. Naresh, R. J. Kumar, K. Chandra Babu Naidu, Ceramics International 45 (2019); https://doi.org/10.1016/j.ceramint.2019.01.044

[22] U. Naresh, R. J. Kumar, K. Chandra Babu Naidu, Materials Chemistry and Physics 236 (2019)121807; https://doi.org/10.1016/j.matchemphys.2019.121807

[23] Liferovich, R. P., Mitchell, R. H. (2005), Physics and Chemistry of Minerals; https://doi.org/10.1007/s00269-005-0020-7

[24] U. Naresh, Rapole Jeevan Kumar, Kadiyala Chandra Babu Naidu, (2019) Bio-interface Research in Applied Chemistry 9, 4243 – 4247; https://doi.org/10.33263/BRIAC95.243247

[25] C. Miclea, C. Tanasoiu, C.F. Miclea, L. Amarande, A. Gheorghiu, F.N. Sima, J. Eur. Ceram. Soc. 25 (2005) 2397-2400; https://doi.org/10.1016/j.jeurceramsoc.2005.03.069

[26] Edelstein, A. S., Everett, R., Perepezko, J. H., Bassani, M., (1997) Journal of Materials Research; https://doi.org/10.1557/JMR.1997.0055

[27] M.P. Zheng, Y.D. Hou, H.Y. Ge, M.K. Zhu, H. Yan, J. Eur. Ceram. Soc. 33 (2013) 1447-1456; https://doi.org/10.1016/j.jeurceramsoc.2012.12.025

[28] Y. Kawamura, N. Matsumoto, H. Kamataki, K. Mukae, Jpn. J. Appl. Phys. 28 (1989) 77-79; https://doi.org/10.7567/JJAPS.28S2.77

[29] Basha, Baba. (2020) Journal of Materials Science: Materials in Electronics. 27. 1-11

[30] R.P. Tandon, V. Singh, N.N. Swami, J. Mater. Sci. Lett. 11 (1992) 327-329; https://doi.org/10.1007/BF00729171

[31] Liu, T., Sun, S., Zhou, L., Li, P., Su, Z., Wei, G. (2019) Applied Sciences, 9(2), 293; https://doi.org/10.3390/app9020293

[32] Wang, Y., Piao, J., Xing, G., Lu, Y., Ao, Z., Bao, N., Ding, J., Li, S., Yi, J. (2015) Journal of Materials Chemistry C; https://doi.org/10.1039/C5TC02936H

[33] Law, C. Sofie, Stephen, (2011) Journal of The Electrochemical Society. 158. B1137; https://doi.org/10.1149/1.3610226

[34] Boysen H, Frey F, Lerch M, Vogt T; (1995) Zeitschr Krystallogr 210:328-337; https://doi.org/10.1524/zkri.1995.210.5.328

[35] Ko J, Prewitt C, (1988) Phys Chem Mineral 15:355-362; https://doi.org/10.1007/BF00311040

[36] Syono Y, Akimoto S, Ishikawa Y, Endoh Y, (1969) J Phys Chem Solids 30:1665-1672; https://doi.org/10.1016/0022-3697(69)90234-0

[37] Sakout, Y., El Ghadraoui, O., Lahrar, E.H. et al., J. Electron. Mater. 53, 141-156 (2024); https://doi.org/10.1016/j.ceramint.2023.11.249

[38] L. Hankey, J. V Biggers, Solid-state Reactions in the System, J. Am. Ceram. Soc. 64 12 (1981) C172 - C173.

[39] M. Hammer, M.J. Hoffmann, J. Am. Ceram. Soc. 81 (1998) 3277-3284; https://doi.org/10.1111/j.1151-2916.1998.tb02768.x

[40] S.R. Shannigrahi, F.E.H. Tay, K. Yao, R.N.P. Choudhary, Effect of rare earth (La, Nd, Sm, Eu, Gd, Dy, Er and Yb) ion substitutions on the microstructural and electrical properties of sol-gel grown PZT ceramics, 24 (2004) 163-170; https://doi.org/10.1016/S0955-2219(03)00316-9